Journal of
Materials Chemistry A

Materials for energy and sustainability

Accepted Manuscript

This article can be cited before page numbers have been issued, to do this please use: Z. L. Moreno Botello, A. Montenegro, N. Grimaldos Osorio, M. Huvé, C. Pirovano, D. R. Småbråten, S. M. Selbach, A. Caneiro, P. Roussel and G. H. Gauthier, *J. Mater. Chem. A*, 2019, DOI: 10.1039/C9TA04912F.

ROYAL SOCIETY OF CHEMISTRY

rsc.li/materials-a

Pure and Zr-doped $YMnO_{3+\delta}$ as YSZ-compatible SOFC cathode: a combined computational and experimental approach.

Zulma L. Moreno Botello[a,b], Alejandra Montenegro[b], Nicolas Grimaldos Osorio[a,c], Marielle Huvé[c], Caroline Pirovano[c], Didrik R. Småbråten[d], Sverre M. Selbach[d], Alberto Caneiro[b], Pascal Roussel[c], Gilles H. Gauthier[a,*]

[a] Universidad Industrial de Santander, Grupo INTERFASE, Ciudad universitaria, Calle 9, Carrera 27, Bucaramanga (Santander), Colombia.

[b] Centro Atómico Bariloche, Comisión Nacional de Energía Atómica, Av. Bustillo 9500, 8400, S. C. de Bariloche, Argentina.

[c] Univ. Lille, CNRS, ENSCL, Centrale Lille, Univ. Artois, UMR8181, UCCS-Unité de Catalyse et Chimie du Solide, Lille, F-59000, France.

[d] Department of Materials Science and Engineering, NTNU Norwegian University of Science and Technology, NO-7491 Trondheim, Norway.

* Corresponding authors: Phone: (+57) 7344000 ext. 2528, Email: gilgau@uis.edu.co (Gilles Gauthier). Phone: (+33) 320434899, Email: pascal.roussel@ensc-lille.fr (Pascal Roussel).

Abstract

A thorough study of the $Y_{1-X}Zr_xMnO_{3+\delta}$ series is presented with the objective to use those materials as SOFC cathode. These pure and Zr-doped yttrium manganites exhibit a layered hexagonal structure associated to a peculiar 5-fold bi-pyramidal coordination of manganese that makes it intrinsically different from the traditional cubic-like perovskite with [MnO_6] octahedra, creating the conditions for a propensity to oxygen uptake at low temperature in the case of the layered manganite. Zr for Y doping enables to maintain such oxygen excess as interstitial atoms Oi located in the equatorial plane of the bi-pyramids. Such overstoichiometric interstitial oxygen sites are clearly evidenced by maximum entropy method (MEM) applied to neutron diffraction data, and Density Functional DFT calculations are used to model the structural accommodation of Zr and excess oxygen. Mn reduction to Mn^{2+} is found energetically unfavourable, as proved both experimentally and using DFT calculations. Hence, zirconium is found to both stabilize excess oxygen compared to

pure $YMnO_3$ as well as possibly providing an oxygen ion migration path with lower energy barrier. The main consequence is a possible MIEC behaviour in Zr-doped $YMnO_3$, as suggest both conductivity measurements and theoretical calculations. First EIS measurements are very promising and rise the series and its original structure to the rank of materials of interest for application as SOFC electrode.

Keywords: Solid Oxide Fuel Cells, Cathode, Zr-doped Yttrium manganite, Electrical conductivity, DFT calculations, Ionic diffusion, Electrochemical Impedance Spectroscopy.

1. Introduction

Solid Oxide Fuel Cells (SOFC), where the electrolyte is a dense ceramic compound conducting O^{2-} ions at high temperatures (T> 600ºC), is one of the most viable solutions for energy production in the future. It can operate either with hydrogen, the non-polluting fuel by excellence, or with any organic fuel (fossil or synthetic), with a higher conversion efficiency than any "classical" technologies [1]. In those systems, the electrolyte is made of Yttria-Stabilized Zirconia (YSZ), which conducts oxide ions from 600 to 1000°C. Ni-YSZ CerMet (Ceramic/Metal composite) is the state-of-the-art anode, offering high catalytic activity and electronic conduction, while transition metal oxides, *e.g.* perovskite-type materials with ABO_3 stoichiometry like Sr-doped $LaMnO_3$, are used as cathode [1] [2] [3]. Designed to operate at temperatures higher than 700 °C, the state-of-the-art materials used to fabricate SOFCs suffer from interface chemical compatibility issues during cell preparation and/or *in operando.* This is especially the case at the cathode side where the main degradation mechanism is interfacial reactions between electrode and electrolyte or interconnect [4] [5] [6] [7] [8] [9] [10]. SOFC cathode materials must also possess high electronic conductivity and sufficient electrocatalytic activity for the oxygen reduction. The latter is generally fulfilled for Mixed Ionic and Electronic Conductors (MIEC) and most of the MIEC materials that have been considered are perovskites [1] [2] [3] [11].

During the last decades, most studies on new cathode materials for SOFC have focused on La/Sr perovskite oxides, while comparatively less attention has been given to other promising materials, *e.g.* the large family of manganites[12] [13] [14].

View Article Online
DOI: 10.1039/C9TA04912F

Here we examine the yttrium manganites for two main reasons: (i) Y is a constitutive element of state-of-the-art YSZ electrolyte, suggesting limited interface degradation and (ii) this particular framework exhibits large oxygen hyperstoichiometry [15] [16] [17]. $REMnO_{3+\delta}$ oxides can crystallize into two distinct structural types, depending on the size of the rare earth (RE) cation with respect to Mn: when the RE ionic radius is large (La-Tb) the structure adopts the "usual" perovskite arrangement, but for smaller species (Dy-Lu, Y, Sc), the material becomes hexagonal and layered [18] [19]. The relative stability of the layered structure with respect to the perovskite is governed by the Goldschmidt tolerance factor *t*. Thus, for small cations, (*i.e.* for $t<0.855$) the hexagonal polymorph is the most stable, while perovskite is stable for higher *t* values [20] [21]. Situated at the crossing-value of the *t*-factor, $YMnO_3$ can be prepared in both structure types. Hexagonal $YMnO_3$ (h-$YMnO_3$, space group $P6_3cm$ is easily obtained by solid-state reaction. *e.g.* at 1200 °C in air under ambient pressure [19]. As depicted in Figure 1a, the structure is built of layers of Y^{3+} ions and MnO_5 trigonal bipyramids [22] [23]. The corner-sharing polyhedra form a triangular network in the basal plane *ab*. Additionally, it is worth mentioning that Y^{3+} layers are "buckled" [24] [25] leading to two non-equivalent Y-sites with two different apical Y-O bond lengths, which causes a tilt of the bipyramids with respect to the *c*-axis [15] [24] [26]. Increasing the temperature up to T~980°C in air, $YMnO_3$ becomes centrosymmetric ($P6_3/mmc$ space group) with non-tilted MnO_5 polyhedra [27] [19] [28] [29].

Recently, it has been observed that $REMnO_{3+\delta}$ compounds with small or intermediate RE^{3+} cations (Y, Dy, Ho, Er or Yb) have the ability to reversibly store different quantities of oxygen and adopt, as a consequence, distinct crystal structures, depending on temperature and/or oxygen pressure. At temperatures higher than T~350°C and in air, those compounds present a low oxygen content ($\delta\sim0$) and adopt the $P6_3cm$ space group. But, in pure O2 and in a narrow temperature range, between 250°C and 350°C, or during slow cooling in the same atmosphere, the materials exhibit a large oxygen uptake (up to $\delta\sim0.25$-0.28), inducing a phase transition to a $R3c$ arrangement, due to a tripling of the *RT* cell along the *c*-axis and presenting six oxygen sites (instead of five in the parent structure). Thus, in this case, a new oxygen site, located in empty hexagonal cavities that defined three MnO_5 bipyramids within the equatorial Mn-O plane of the parent $P6_3cm$ structure, is partially filled by over-stoichiometric oxygen (Figure 1b). In that way, the extra oxygen atoms induce a rearrangement in the stacking model of the

View Article Online
DOI: 10.1039/C9TA04912F

Mn-O layers and Mn trimers are no more located exactly on top of each but are shifted by 3/2 1/3 $C_h/2$ (in the hexagonal setting) [16] [30]. After annealing at 190 bar of oxygen pressure, the oxygen content can increase up to δ≈0.40 and at this point the structure transforms into another supercell with *Pca2₁* space group [31]. In this last orthorhombic arrangement, similarly to the aforementioned rhombohedral superstructure, but with lower symmetry, the oxygen excess is located in several partially filled sites within the same hexagonal cavities of the Mn-O layers, giving Mn atoms a higher coordination (an example of 8-fold coordination for one of the three Mn sites is given in Figure 1c). [16] Therefore, considering that some of the original equatorial sites of the MnO_5 polyhedra are now partially empty and that new interstitial positions (with possibly higher energy) are, in change, partially occupied too, such situation seems to create perfect conditions for oxygen atoms to move easily within the structure. The mobility of oxygen ions is a crucial point in the search of MIEC compounds [32]. In Figure 1d, the simulated X-Ray diffractograms of the aforementioned structures are given for comparison. Even if the diffraction patterns of the four structures are very similar, especially in the more intense reflections regions (2θ~28-35°), the pattern of the rhombohedral structure shows a greater number of peaks, and the presence of the super-reflection at 2θ~23° in the $P6_3cm$ pattern distinguishes it from the $P6_3/mmc$ structure.

Zirconium can be substituted for yttrium in h-$YMnO_3$, forming a solid solution [33] [34]. van Aaken *et al.* affirm that such substitution is possible up to 30 % [33], while Katsufuji *et al.* obtained single phased $Y_{1-x}Zr_xMnO_3$ (YZM) materials only up to x=0.1 [34]. In a previous work, our team confirmed solubility limit around x=0.1 using solid-state synthesis route [35] as well as chemical and thermomechanical compatibility of YZM with YSZ electrolyte material, making this material of strong interest for application as SOFC cathode. In this work, we present an in-depth structural characterization of $Y_{1-x}Zr_xMnO_{3+\delta}$ compounds, prepared by a sol-gel Pechini-type route, and addressing in particular the charge equilibrium in the Zr-doped compounds. Moreover, the electrical and electrochemical properties of the compounds are described and discussed, confirming their potential as cathode component in Solid Oxide Fuel Cells. Finally, a detailed DFT study is carried out to model the structural accommodation of Zr and excess oxygen as well as the electronic and ionic properties of these materials.

View Article Online
DOI: 10.1039/C9TA04912F

2. Experimental and Methods

2.1 Materials synthesis

Pure and Zr-doped yttrium manganites of compositions $Y_{1-x}Zr_xMnO_3$ (x=0, 0.05 and 0.1) were prepared by solid-state reaction using the following precursors: Y_2O_3 (Alfa Aesar, 99.9%, dried at 1000 ºC for 3 h), MnO_2 (Alfa Aesar, 99.9%, dried at 150 ºC for 3 h) and ZrO_2 prepared by treating Zirconium(IV) isopropoxide (Alfa Aesar, 99.9%) at 1000 ºC for 3 h. Stoichiometric amounts of the corresponding powders were weighed, mixed and ground together before being pressed into pellets that were placed on alumina or platinum foils with a sacrificial powder bed, then heat treated in air one or several times depending of the composition: for x=0, the thermal profile was only T=1400 ºC for 12 h and, for the other compositions, at T=1400 ºC, 1450 ºC and finally 1500 ºC, each time for 12 h, with intermediate grinding and re-pelletizing between each step to obtain high purity samples (heating and cooling rates = 4 ºC min^{-1}).

As an alternative synthesis technique, the materials were also prepared using the Pechini route where metal precursors in the form of nitrates, carbonates and oxides were used to synthesize the compounds (Y_2O_3, 99.9%, Alfa Aesar; $MnCO_3$, 99.99 %, Sigma Aldrich; $ZrO(NO_3)_2.H_2O$, 99.9 %, Alfa Aesar; $C_{12}H_{28}O_4Ti$, 99.995 %, Alfa Aesar). First, the stoichiometric quantities of the reactants were dissolved in nitric and citric acid with a minimum quantity of water until a homogeneous solution was obtained (T=80°C). Ethylene glycol was added to this mixture and the temperature (T>100°C) was raised to induce the formation of a polyester, while the water evaporates. Once the polymerization completed, a highly viscous organic mass (gel) was formed. Subsequently, the gel was calcined at 300 and 500°C (for 5 hours) to decompose the organic species. Finally, the powder was pressed into pellets which were thermally treated in air, on sheets of alumina, at 1100 °C ($YMnO_3$) or 1200°C (Zr-doped samples) for 12 hours, with a heating ramp of 5°C min^{-1}.

2.2. Structure and oxygen stoichiometry determination

Phase analysis was performed after synthesis by X-ray diffraction at room temperature using a BRUKER D8 ADVANCE powder diffractometer working in Bragg

Brentano geometry with Cu-Kα radiation and a 1D LynxEye detector. The diffractometer was operated over the angular range 2θ=10-70° for qualitative analysis and 2θ=10-140° for Rietveld analysis, using a step size of 0.015° in 2θ and acquisition time of 1 s per step. Crystal structure refinements were performed by the Rietveld method using the FullProf software [36] and its graphical interface WinPLOTR [37]. In this case, the background was fitted with a 6-coefficient polynomial function. A pseudo-Voigt function was used to model profile shapes, including the Cagliotti function variables U, V, W, the Gaussian-Lorentzian mixing parameter η and two low theta asymmetry parameters. The values of standard deviations were corrected according to Berar and Lelann's description [38].

Neutron powder diffraction (NPD) measurements were carried out at the Orphée reactor of the Leon Brillouin Laboratory (CEA/Saclay-France), on the high resolution 3T2 diffractometer. A Ge(335) monochromator was used to select a wavelength of 1.228 Å. The data analysis was performed by the Rietveld method using the Jana2006 program [39]. Coupled refinements (neutrons and X-ray) were also conducted.

Maximum Entropy Method (MEM) nuclear densities have been computed with the Dysnomia 0.9 program [40] using F-constraints, uniform prior densities and a zeroth-order single pixel approximation (ZSPA) algorithm. 92 observed structure factors were extracted according to Rietveld refinements against powder data carried out with the Jana2006.

Electron diffraction patterns were obtained on a FEI Technai G2-20 twin transmission electron microscope. The powder was crushed, and the alcoholic suspension deposited on carbon supported grid followed by evaporation under ambient conditions.

Thermogravimetric analysis was undertaken in different atmospheres (anodic and cathodic) to follow mass variation following several thermal treatments. Essentially, the thermobalance consists of custom-built high precision Cahn electrobalance 1000 (±10 μg) [41] and a temperature-controlled oven (20-1000°C). The same gas is made to flow through both sides of the balance. The experiments were carried out in air (flow of 80 mL min^{-1}) from room temperature to 900°C (with heating/cooling ramp rates of 0.2°C min^{-1}). Additionally, the samples were exposed to a 50%H_2/Ar (flow of 80 mL min^{-1}) reducing atmosphere until the material was decomposed to its initial reagents, so that it was carried out up to 900°C or even

View Article Online
DOI: 10.1039/C9TA04912F

1000°C (with ramp rates of 5°C min^{-1}) if the sample proved to be very stable. After this cycling procedure, the change in the absolute oxygen stoichiometry ($3+\delta$) of the $ABO_{3+\delta}$ compound under all conditions, was calculated taking into account the corresponding products of the decomposition, *i.e* Y_2O_3 and MnO in the case of $YMnO_{3+\delta}$.

2.3. Electrical conductivity measurements

Total electrical conductivity measurements were performed in air by four-probe DC technique, using a BioLogic SP-300 Potentiostat-Galvanostat. For such purpose, dense cylindrical samples (~4 mm in diameter and ~8 mm in length) were first prepared from the corresponding powder (Pechini synthesis) isostatically pressed at 1800 bar then sintered at 1350 °C for 2 h, leading to pellets with ~90-95% relative density. The measurements were performed in air from 850 °C to 400 °C using gold wires and gold paste for contacts. All the conductivity values were corrected from porosity according to the equation proposed in [42].

2.4. Electrochemical measurements

Electrochemical Impedance Spectroscopy (EIS) of symmetrical cells in air were used to evaluate the electrocatalytic behaviour of the materials for oxygen reduction. Pellets (~ 1 cm diameter) of commercial Yttria-Stabilized Zirconia (TZ-8Y, Tosoh Corporation) were sintered at 1300°C for 6 h (heating and cooling ramp rates of 3.5°C.min^{-1}). Then, the electrode material and the current collectors were deposited by spin coating with the aim of achieving a porous microstructure. Each ink was prepared by mixing isopropanol with the electrode material and Polyvinyl Butyral (1.7 wt.% - binder) and Polyvinylpyrrolidone (0.9 wt.% - dispersant) until the alcohol evaporates. Subsequently, alpha terpineol (23.6 wt.%) and isopropanol (38.8 wt.%) as co-solvents were added to the powder, until complete dispersion. After preliminary optimization, the best results were obtained for LSM/YZM/YSZ/YZM/LSM symmetric cells where LSM stands for the "classical" $La_{0.2}Sr_{0.8}MnO_3$ cathode material, used here as current collector. After optimization, thicknesses of LSM and YZM were set to 10 and 20 µm, respectively. Those symmetric cells were submitted to a sintering heat-treatment at 1150 and 1100 °C for 3h in air in the case of pure and Zr-doped

View Article Online
DOI: 10.1039/C9TA04912F

$YMnO_3$, respectively. The EIS spectra were obtained with a frequency response analyser (FRA2) connected to a potentiostat AUTOLAB PGSTAT30 (EcoChemie). The measurements were carried out in a frequency range of 1MHz to 1mHz, with an alternating voltage (amplitude 10mV) and zero Bias voltage, in the temperature range of 500-800°C. The data were adjusted by least squares method with equivalent circuits using the software ZView® (Scribner Associates, Inc.).

2.5. Density functional theory (DFT) calculations

Density functional theory (DFT) calculations were carried out with VASP [43 44 45] using the PBEsol functional [46]. In the present study Y (4*s*, 4*p*, 5*s*), Mn (3*s*, 3*p*, 3*d*, 4*s*), O (2*s*, 2*p*) and Zr (4*s*, 4*p*, 5*s*, 4*d*) were treated as valence electrons. 120 atoms 2x2x1 supercells were used as model systems. One Zr-dopant and/or one oxygen interstitial per supercell were assumed, with the resulting stoichiometries of $YMnO_{3+\delta}$ and $Y_{1-x}Zr_xMnO_{3+\delta}$ with x=δ=0.042. The plane-wave energy cut-off was set to 550 eV, and the Brillouin zone was integrated over a Γ-centred 2x2x2 *k*-point density for geometry optimization and 4x4x4 *k*-point density for electronic density of states (DOS) calculations. Lattice parameters and positions for the undoped and doped systems where relaxed until the residual forces on all the ions were below 0.005 eV $Å^{-1}$. The lattice parameters for the oxygen rich supercells were fixed to the relaxed values of corresponding oxygen stoichiometric supercells. To reproduce the experimental lattice parameters [19] and band gap [47], GGA+U [48] with U=5 eV on Mn 3d was used, with the collinear frustrated antiferromagnetic order [49] on the Mn sublattice. For the structural accommodation of Zr-dopants and oxygen excess, both 120 atoms 2x2x1 supercells and 30 atoms unit cells were investigated. Here, the lattice parameters for the oxygen excess supercells were also allowed to relax. For the 30 atoms unit cells, the *k*-point density was increased to 4x4x2. The defect formation energies of oxygen interstitials were calculated as

$$E^f_{O_i''} = E_{def} - E_{ref} - \mu_O \quad (1)$$

where E_{def} and E_{ref} are the total energy of the oxygen rich and oxygen stoichiometric supercells, respectively. μ_O is the chemical potential of oxygen, varying within the DFT calculated stability region [50] of $YMnO_3$ between –7.1 and –1.9 eV. The oxygen interstitial migration energy barriers were determined from climbing image nudged

View Article Online
DOI: 10.1039/C9TA04912F

elastic band (c-NEB) calculations [51] [52], with five intermediate images between the initial and final structure. Each intermediate image was relaxed until the residual forces on all ions were below 0.3 eV $Å^{-1}$, with a spring constant of 5 eV acting between the images.

3. Results and discussion

3.1. Structure and charge compensation in the Zr-doped $YMnO_3$ series

Our previous preliminary results on the synthesis of $Y_{1-x}Zr_xMnO_{3+\delta}$ (x=0-0.15) materials using the solid-state technique and high temperatures up to 1500°C, described in [35], confirmed that pure materials with the expected *P*6_3*cm* hexagonal space group can be obtained for substitutions levels up to x=0.1. As shown in Figure 2, for x=0.15, a YSZ-type impurity was clearly evidenced, contradicting the results obtained by Van Aken *et al.* [33], but in agreement with Katsufuji *et al.* [34]. Results from Rietveld refinement of the data in Figure 2 are given in section 1 of Supplementary Information. For $YMnO_3$, the refined values of lattice parameters were close to those obtained by other authors [19] [33]. Due to Zr substitution for Y, the cell volume dramatically drops along with x in $Y_{1-x}Zr_xMnO_{3+\delta}$ series, as a result of a strong decrease in the *c* lattice parameter. Meanwhile, the *a* parameter remains about the same. In a first approximation, the decrease of the volume for the substituted compounds was attributed to the fact that a fraction of the Y^{3+} cations (r_{Y3+}=1.019 Å) is replaced by smaller Zr^{4+} cations (r_{Zr4+}=0.84 Å) [53]. Nevertheless, such justification was not completely satisfactory, as Zr-doping necessarily induces a charge compensation, which must be also taken into account. A first hypothesis was to consider that the charge equilibrium occurs according to the following reaction, written in Kröger-Vink notation, in which Mn_{Mn}^{X} and $Mn_{Mn}^{'}$ means Mn^{3+} and Mn^{2+} cations at the manganese crystallographic site in $YMnO_3$ [35]:

$$Y_Y^X + Mn_{Mn}^X + 3O_O^X + ZrO_2 \rightarrow Zr_Y^{\bullet} + Mn_{Mn}^{'} + 3O_O^X + {}^1/_2 Y_2O_3 + {}^1/_4 O_2 \qquad (2)$$

In this hypothesis, the charge balance due to Zr-doping is achieved when part of the Mn^{3+} cations is reduced to Mn^{2+} [34] [54]. Considering that the latter cation has a greater ionic radius than Mn^{3+} (r_{Mn3+}=0.58 Å and r_{Mn2+}=0.75 Å) [53], it becomes clear that the

View Article Online
DOI: 10.1039/C9TA04912F

change of the transition metal-ionic size by itself does not explain the observed data, unless the effect is negligible with respect to the already discussed direct size effect due to Zr for Y substitution.

Another hypothesis is to consider that Zr^{4+} donor doping is not compensated by manganese reduction, but by excess interstitial oxygen, as described by the following equation:

$$Y_Y^X + Mn_{Mn}^X + 3O_O^X + ZrO_2 \rightarrow Zr_Y^\bullet + Mn_{Mn}^X + 3O_O^X + {}^1/_2\, Y_2O_3 + {}^1/_2\, O_i'' \qquad (3)$$

In order to discriminate between the two hypotheses, the absolute oxygen content (3+δ) of as-synthesized $Y_{0.9}Zr_{0.1}MnO_{3+\delta}$ sample was determined during a thermal cycle in air. For this purpose, the sample mass was followed by TGA measurement in air before the material was completely decomposed to the corresponding precursors, *i.e.* Y_2O_3, ZrO_2 and MnO, during a second cycle in 50%H_2/Ar (not shown). The results of such experiments are depicted in Figure 3. δ slowly decreases from 0.05 at room temperature to 0 for T>600 °C, going through a small oxygen uptake around T=200 °C in the case of $YMnO_{3+\delta}$. The Zr-doped sample exhibits a similar but stronger behaviour: the 3+δ value is ~3.05 at temperatures higher than 650°C in air. Such result allows discarding the first hypothesis (Eq. *2*), since the oxygen content of the compound perfectly fits with $Y_{0.9}^{+3}Zr_{0.1}^{+4}Mn^{3+}O_{3.05}^{-2}$ formula and not $Y_{0.9}^{+3}Zr_{0.1}^{+4}Mn_{0.9}^{3+}Mn_{0.1}^{2+}O_{3.0}^{-2}$, supporting the second hypothesis (Eq. *3*). The deduced oxygen content value 3.1 before TGA measurements (*i.e.* after synthesis) confirms the second charge equilibrium mechanism and we may conclude that the initial stoichiometry of the Zr-doped material is indeed $Y_{0.9}^{+3}Zr_{0.1}^{+4}Mn_{0.9}^{3+}Mn_{0.1}^{4+}O_{3.1}^{-2}$, due to the fact that a small fraction of Mn^{3+} cations is oxidized to Mn^{4+}, in addition to the oxygen excess due to Zr-doping. The latter oxygen uptake, present at low temperature in air, corresponds to the following (simplified) equation:

$$Mn_{Mn}^X + {}^1/_4\, O_2 \leftrightarrow Mn_{Mn}^\bullet + {}^1/_2\, O_i'' \qquad (4)$$

On cooling, specifically from T=400 down to 200°C, the compound shows a mass uptake, related to manganese oxidation, with a maximum oxygen content of ~3.21. The final material stoichiometry, reached after TGA, is $Y_{0.9}^{+3}Zr_{0.1}^{+4}Mn_{0.68}^{3+}Mn_{0.32}^{4+}O_{3.21}^{-2}$ *i.e.* with greater oxygen amount than after synthesis. In summary, we can clearly see that Zr-doped $YMnO_3$ can absorb/desorb in air different amounts of oxygen,

View Article Online
DOI: 10.1039/C9TA04912F

depending on the temperature. This behaviour seems common to all $RMnO_3$ hexagonal manganites, including $YMnO_3$, as discussed in the introduction. However, as clearly shown in Figure 3, the storage capacity is much higher for $Y_{0.9}Zr_{0.1}MnO_{3+\delta}$ than for $YMnO_{3+\delta}$. For such Zr-doped compounds, the oxygen content significantly raises in air (~3.21) and reaches values that are similar to those observed under severe conditions for non-doped $YMnO_3$ (~3.13 by very slow cooling in pure oxygen and ~3.36 after high-pressure oxygen annealing at 190 bar at 400°C) [16].

To further study the difference of oxygen uptake behaviour of pure and Zr-doped $YMnO_3$ materials and, at the same time, obtain them at lower temperature in view of their use as oxygen reduction electrocatalysts, the classic solid-state technique was replaced by the Pechini method with heat treatment at 1100 °C and 1200 °C for $YMnO_3$ and $Y_{0.9}Zr_{0.1}MnO_3$, respectively. The corresponding X-ray diffractograms are plotted in Figure 4. Sol-gel $YMnO_3$ exhibits the same pattern than the sample prepared by the solid-state method, *i.e.* a structure corresponding to the $P6_3cm$ space group (a~6.14 Å, c~11.38 Å) while $Y_{0.9}Zr_{0.1}MnO_3$, as clearly indicated by the disappearance of the (102) super-reflection located at 2θ≈23°, is correctly indexed in the $P6_3/mmc$ cell with a~3.55 Å and c~11.25 Å. These modifications confirm not only the efficiency of the Pechini method to obtain pure materials at lower temperature, but also that the structure has changed with the addition of Zr. The lattice parameters of both materials, refined using the LeBail method, are listed in section 2 of Supplementary Information, in which the corresponding values of lattice parameters in $P6_3cm$ structure ($a' = \sqrt{3}*a$) are also given for $Y_{0.9}Zr_{0.1}MnO_3$, simplifying the comparison with $YMnO_3$. Beyond the decrease of the c parameter and lattice volume, already observed and discussed for the samples prepared by solid-state synthesis, Zr-doped $YMnO_3$ adopts a $P6_3/mmc$ space group. Such behaviour has already been observed in a close compound (but doped with Ti on the Mn site, instead of Zr on the Y site in our case): the *(102)* super-reflection at 2θ≈23°, present for the pattern of the as-prepared sample, disappears with the oxygen uptake at high temperature [32]. Thus, it is possible to infer that the structural change in our $Y_{0.9}Zr_{0.1}MnO_{3+\delta}$ can be also associated with an oxygen uptake, as evidenced by TGA.

In order to establish where these oxygens atoms are located in the structure and why the structure turns more symmetrical, Neutron Diffraction (ND) analysis was carried out for as-synthesized Zr-doped $YMnO_3$. Using Full Pattern Matching/LeBail

refinement, the neutron diffraction pattern can be indifferently indexed using either *P*6$_3$*cm* or *P*6$_3$*/mmc* space groups, with similar, good R-factors. However, using the literature data for atomic positions, the corresponding Rietveld refinements yield high values of reliability factors in both cases (see details in section 3 of Supplementary Information). Performing difference Fourier maps in either one or the other space group, additional nuclear density around Mn atoms was found, attributed to the expected extra-oxygen. A clear agreement factor decrease was obtained after the addition, and the refining of the occupancy, of the supplementary O3 oxygen atoms leading to the chemical formula $Y_{0.9}Zr_{0.1}MnO_{3.22}$, in the *P*6$_3$*/mmc* structure. Finally, as the anisotropic atomic displacement parameter of the Y-Zr site ((0 0 0), *2a* Wyckoff site) was very elongated along the c direction, this site was split into a half-occupied *4e* Wyckoff position (0 0 0+δ). It is worth noting that all refinements were tested, not only in the *P*6$_3$*/mmc* space group, but also in the less symmetric *P*6$_3$*cm* model. However, the same conclusions were given, *i.e.* supplementary oxygen position and similar agreement factors. In addition, in this later space group, restriction on atomic positions was necessary to achieve convergence, as often observed when a too-low symmetry is used. As a basic rule of crystallography, between two models having same agreement factors, the simplest model was chosen, *i.e.* the *P*6$_3$/*mmc* over-stoichiometric structure. To be absolutely certain, we also tried refinements using the other two models described in literature and mentioned in the introduction for oxygen over-stoichiometric compounds, *i.e.* with space groups *R*3*c* and *P*ca2$_1$, respectively [19] [33]; the results were exactly the same than with hexagonal *P*6$_3$/*mmc* cell, and the conclusions also. Finally, to take advantage of the complementary between the radiations, *i.e.* a good sensitivity of heavy cations for X-ray and a good sensitivity of light anions for neutrons, a coupled Rietveld refinement using both ND and XRD was performed in the *P*6$_3$*/mmc* space group. Graphical result is shown in section 3, index g) of Supplementary Information, while the corresponding structural parameters are listed in Table 1.

Model-free experimental nuclear density maps were calculated from the Maximum Entropy Method combined with Rietveld refinement against neutron diffraction data. A grid step of ~0.07 Å along each direction of the unit-cell was used to describe the nuclear density (the number of voxel in the unit cell was 331776, *i.e.* 48x48x144 for lattice parameters a=3.552 Å and c=11.261 Å. Full convergence was obtained, leading to R_{MEM}=3.44% in the final state. The main advantage of MEM

View Article Online
DOI: 10.1039/C9TA04912F

compared to usual Fourier syntheses lies in the much smaller truncations errors leading to much more accurate nuclear density maps. In addition, since there is no parametrization of the nuclear density, there is no problem of correlation between refined parameters, as we observed if the space group is incorrect for the classical approach. In addition to the disorder previously observed on the Y-Zr site, interstitial oxygen atoms O3 are clearly located in the nuclear density MEM maps (see section 4 in Supplementary Information, showing the 3D iso-density volumetric data treated with VESTA [55]).

Transmission Electron Microscopy, in diffraction mode, was also used to characterize those samples, since this technique is well known to be very sensitive to oxygen stoichiometry deviations through the appearance or disappearance of superstructure reflections (see for instance [56]). The reconstruction of the reciprocal space as well as the comparison between the zero order Laue zone and the first order Laue zone lead to a hexagonal cell a≈6.1 Å and c≈11.3 Å and a partial extinction symbol P.c., compatible with the expected $P6_3cm$ space group. However, some additional phenomena have also been observed on selected area electron diffraction (SAED) patterns (see section 5 of Supplementary Information). Weak streaks (oval in Figure (a) of section 5 in SI) as well as rows of weak spots (arrows in Figure (b) of section 5 in SI) not considered up to now are highlighted showing that the actual situation is in fact more complex. It is however difficult to go further using only SAED since it has been previously shown, on compounds of the same type, that electron beam irradiation can drive the motion of oxygen vacancy under the vacuum environment of a transmission electron microscope and that different ordered arrangements and high mobility of oxygen vacancies depending on the beam-dose can be identified [22]. Energy loss near edge structure (ELNES) studies of oxygen K edge have indeed shown a clear evolution of the spectra after 2 minutes in the TEM interpreted as a decreasing of oxygen content in the irradiated region.

It is worth noting that additional oxygen in the $P6_3/mmc$ SG was clearly evidenced with the sample prepared by Pechini technique, and not by solid state synthesis, probably evidencing the importance of the powder microstructure (grain size in particular) on the kinetics of oxygen absorption, making it difficult to observe in our first experiments [35]. Cooling rate and, in this case, characteristic diffusion length often determines at what temperature equilibration with the atmosphere is no longer retained and the oxygen content effectively 'freezes in'. [57]

As can be seen in Table 1, excess oxygen, namely O3, is located in a *6h* Wyckoff position at the same z-values as for O2-atoms (z=1/4 and 3/4), *i.e.* in the basal planes of the MnO_5 trigonal bipyramids. Exactly as for *R3c* and *Pca*2_1 superstructures described in literature, the excess oxygen is accommodated in the hexagonal interstices formed by three bipyramids, normally empty, as depicted in Figure 5. Such phenomenon is possible because, in $YMnO_3$, as in the Zr-doped structure, the basal oxygens of MnO_5 bipyramids are under-bonded with Mn and, consequently, can easily move in the lattice [32]. Thus, in presence of an oxidizing atmosphere and temperature, these basal oxygen atoms can move in the Mn-O plane filling triangular interstitials sites of the trimers [50]. As a result, Mn cations can virtually increase their coordination and form polyhedra different from the original trigonal bipyramids, similar to what happens in the hyperstoichiometric $RMnO_{3+\delta}$ structures with of *R*3*c* and *P*c$a2_1$ space group [16].

At this stage, we can say that the amount of incorporated excess oxygen in pure $YMnO_{3+\delta}$ is very low in air, as evidenced by TGA measurements. Consequently, the material retains *P*6_3*cm* symmetry for both investigated synthesis routes. This is in agreement with literature in which higher oxygen content values (and the different structure types related to the presence of oxygen atoms in interstitial sites) have been described for pure $YMnO_{3+\delta}$ only in specific conditions of sample cooling in pure oxygen (δ~0.13) or annealing in high pressure O_2 (δ~0.36), *i.e.* far from the SOFC cathode conditions [16]. However, doping $YMnO_{3+\delta}$ with Zr can induce a less distorted structure also associated with a much larger oxygen excess after air cooling. Such behaviour is in part related to an intrinsically higher oxygen content in the doped Zr-sample at all investigated temperatures (*i.e.* even in the temperature range of an SOFC with T>500 °C), but the small oxygen excess (δ=0.05) directly due to the 10% zirconium doping at the Y site alone cannot explain the high oxygen in air regardless of synthesis route (δ~0.25 by slow cooling using TGA measurements for the solid state sample and δ~0.22 after natural cooling using Pechini synthesis). The observed higher propensity of $Y_{0.9}Zr_{0.1}MnO_{3+\delta}$ to oxygen uptake compared to pure $YMnO_{3+\delta}$ must have a thermodynamic and/or kinetic origin, where the latter can be rate limited by oxygen surface exchange or bulk diffusion. This point will be further discussed below. Finally, it is worth noting that the doped samples obtained by solid-state and Pechini route have the same crystal structure, but oxygen absorption and desorption

View Article Online
DOI: 10.1039/C9TA04912F

is faster for the Pechini route material, which also exhibits a higher oxygen content as-prepared than the solid-state material. We attribute this difference to the smaller grain size of the Pechini route material, implying shorter diffusion distances between interior bulk and surface during oxygen exchange.

To provide a more fundamental understanding of the experimental observations, we have determined how Zr-doping and oxygen excess through oxygen interstitials (O_i) affect the structural parameters and the energetics using density functional theory (DFT) calculations. The calculated changes in structural parameters for different stoichiometries are summarized in section 6 of Supplementary Information. Zr-doping intrinsically gives decreased cell volume with increasing Zr-content, caused by a strong contraction of both the *a* and *c* lattice parameters. Oxygen excess, on the other hand, gives an increased cell volume with increasing oxygen content, caused mainly by a strong expansion of *a* lattice parameter. This suggest that the oxygen rich $Y_{1-x}Zr_xMnO_{3+\delta}$ should show a decrease in the cell volume with increasing Zr- and O-content, caused by a strong contraction of the *c* lattice parameter, and either an unchanged or a weak expansion of *a* lattice parameter. This is indeed apparent from the structural parameters for oxygen rich $Y_{1-x}Zr_xMnO_{3+\delta}$ (section 6 in SI), where the reduced cell volume with increasing x and δ is caused by an expansion of *a* lattice parameter and a contraction of *c* lattice parameter. These results are in good agreement with the XRD results for the as-prepared samples, further supporting that they should be oxygen rich. Note that the chemical expansion of the *a* lattice parameter as a function of O_i concentration is non-linear (see the table in section 6 of Supplementary Information). The introduction of an interstitial site will naturally expand the crystal lattice, however the corresponding charge compensation of a negatively charged O_i comes with the oxidation of Mn^{3+} to Mn^{4+}. As the latter is a smaller cation, the net effect of the interstitial site expansion and the chemical contraction is the observed non-linearity.

The superior oxygen storage capacity for $Y_{0.9}Zr_{0.1}MnO_{3+\delta}$ compared to $YMnO_{3+\delta}$ can be elaborated by the calculated defect formation energies of forming oxygen interstitials in $Y_{1-x}Zr_xMnO_{3+\delta}$ and in $YMnO_{3+\delta}$ (x=δ=0.042) in Figure 6a. The oxygen interstitial formation energy is found to be ~0.8 eV lower in the Zr-doped systems. This can be reasoned from how the oxygen interstitials are charge compensated in $YMnO_{3+\delta}$ and $Y_{1-x}Zr_xMnO_{3+\delta}$. In $YMnO_{3+\delta}$, the oxygen interstitials are

View Article Online
DOI: 10.1039/C9TA04912F

charge compensated according to Eq. (4), while in $Y_{1-x}Zr_xMnO_{3+\delta}$ (assuming x=δ) the oxygen interstitials are charge compensated, by combining Eqs. (3) and (4), according to:

$$Y_Y^X + Mn_{Mn}^X + 3O_O^X + ZrO_2 + \frac{1}{2}O_2 \rightarrow Zr_Y^{\bullet} + Mn_{Mn}^{\bullet} + 3O_O^X + \frac{1}{2}Y_2O_3 + O_i'' . \quad (5)$$

The oxygen interstitials in $Y_{1-x}Zr_xMnO_{3+\delta}$ are hence charge compensated by oxidizing only one Mn^{3+} to Mn^{4+}, compared to two Mn^{3+} in $YMnO_{3+\delta}$, which should explain the lower formation energy in the former. Charge compensation of Zr^{4+} in $YMnO_3$ by reduction of Mn^{3+} to Mn^{2+} requires population of the high-energy $3d_z^2$ orbitals of Mn, similar to the charge compensation mechanism for oxygen vacancies. [58], which further explains why excess oxygen is the energetically preferred charge compensation mechanism for Zr^{4+} donor doping on the Y^{3+} site. In addition, the energy lowering can also be reasoned from the difference in bonding between O_i and Y or Zr. From the DFT relaxed structures, we find bond lengths for Y1-O_i and Y2-O_i of 2.29 Å and 2.42 Å, respectively, in undoped $YMnO_{3+\delta}$, while in $Y_{1-x}Zr_xMnO_{3+\delta}$ we find corresponding bond lengths of 2.15 Å and 2.24 Å for Zr_{Y1}-O_i and Zr_{Y2}-O_i, respectively. The O_i interstitials are thus more tightly bound to the Zr-dopant compared to the corresponding Y in $YMnO_{3+\delta}$, which gives an additional stability and an energy lowering of forming O_i in $Y_{1-x}Zr_xMnO_{3+\delta}$.

3.3. Electrical properties

The electronic properties of the $Y_{1-x}Zr_xMnO_{3+\delta}$ series can be predicted from a defect chemistry model with respect to oxygen content, *i.e.* oxygen partial pressure during thermal treatment. In sufficiently low pO_2, assuming oxygen stoichiometry δ=0, the material should be n-type conducting according to Eq. (2), where the n-type conductivity arises from the charge compensation of Zr^{4+} by reducing Mn^{3+} to Mn^{2+}. For sufficiently high pO_2, the material should become p-type conducting according to Eq. (5), where the p-type conductivity arises from the charge compensation of O_i by oxidizing Mn^{3+} to Mn^{4+}.

These charge compensation mechanisms are confirmed by the calculated electronic density of states (DOS) in Figure 6b. The top panel shows the atom-resolved DOSes for stoichiometric $YMnO_3$, where the valence band consists mainly

View Article Online
DOI: 10.1039/C9TA04912F

of O 2*p* states, and the conduction band mainly of Mn 3*d* states, separated by a band gap of ~1.5 eV. The addition of an oxygen interstitial (second panel) results in an unoccupied defect state in the band gap of mostly Mn^{4+} ($3d_{xy}$,$3d_{x2-y2}$) and O ($2p_x$, $2p_y$) character, and binding states between Mn^{4+} and O_i at the bottom of the valence band edge, in accordance with Skjærvø *et al.*. [58] Adding a Zr-dopant (third panel) shifts the Fermi level into the conduction band, where the occupied states are of mainly Mn $3d_{z2}$ character. Finally, by adding an oxygen interstitial to the Zr-doped system (bottom panel), the Fermi level is shifted back to the valence band edge, with the emergence of binding states between Mn^{4+} and O_i, as for O_i in undoped $YMnO_3$. For simplicity, only the results for $Zr_{Y2}^{\bullet}$-doping is shown. Similar results are also observed for $Zr_{Y1}^{\bullet}$-doping.

The evolution in air of the resistivity with temperature was measured by 4-points probe technique for each sample (Figure 7a). Note that these measurements were carried out on the samples obtained by Pechini method, since the obtained microstructure is favourable for the oxygen absorption. For both materials, the conductivity increases in a similar way when the temperature raises, exhibiting a semiconducting behaviour [59] However, the Zr-doped sample shows much higher conductivity level than the pure yttrium manganite. By comparison to previously reported works for $YMnO_3$ (*e.g.* σ=2x10^{-3} S cm^{-1} in Remsen *et al.* [58], σ=3.5x10^{-3} S cm^{-1} in Jeuvrey *et al.* [59] or σ=3.16x10^{-3} S cm^{-1} in Ismailzade *et al.* [60] at 750 °C in air), our measurements show slightly higher electrical conductivity (*e.g.* σ=7.4x10^{-3} S cm^{-1} on the same conditions); however, it is in the same order of magnitude. This small difference may be due the fact that, in our case, compacity (or porosity) corrections (which take into account the deviation to fully dense sample) were applied, while such kind of corrections are not mentioned in the previously mentioned articles [60] [61] [62]. $YMnO_3$ can be described as a semiconductor, and more specifically a p-type conductor [27] [59] [63], as other hexagonal manganites with small rare-earth cations at the A-site (Er, Tm, Yb, Lu and Y). In those materials, the conductivity is mainly due to the partial oxidation of Mn^{3+} to Mn^{4+}, which corresponds to the formation of electron holes [24] [32]. Particularly, this could be related to the above described extra interstitial oxygen atoms, a fraction of occupied Mn *d* states closest to the Fermi energy being lifted above E_F on inclusion of O_i as electron density is donated from Mn 3*d* (Mn^{4+} $d_{x^2-y^2}$) to O 2*p* ($2p_x$ and $2p_y$). Although the charge transfer is not complete, this is

View Article Online
DOI: 10.1039/C9TA04912F

regarded as the oxidation of Mn^{3+} to Mn^{4+} [50]. Therefore, holes are created in the valence band and induces p-type conductivity. The conduction process consists of small polarons formation and their movement between the Mn^{3+} and Mn^{4+} sites according to a hopping mechanism [27 59 61 63]. It is worth remembering that most of the manganese oxides of perovskite structure (ABO_3) conduct electricity by such kind of mechanism, given that the radius of the particle is comparable to the interatomic distances of the oxide[64]. Therefore, even if the crystal structure is not the same, it is not surprising that hexagonal $YMnO_3$ exhibits the same behaviour. In addition, the reported low drift mobility of the positive carriers (μ=3 x 10^{-6} cm^2 V^{-1} s^{-1} at 500°C), characteristic of moving holes along localized levels, and the positive sign of Seebeck coefficient (p-type electronic conduction) [50 65] support those previous statements. In order to calculate the activation energy of the hopping process, ln(σT) was plotted as a function of 1000/T and the corresponding Arrhenius curve is given in Figure 7b. As observed in Figure 7, the values fit very well to this linearization, confirming that the materials are narrow band semiconductors in which small polarons are moving [63]. Additionally, we can observe that for both materials, the conductivity exhibits a change of slope around T=550°C, meaning two different regimes, at low (LT) and high temperature (HT), respectively. Calculated activation energies in the two temperature regions are given in Table 2 and compare well to literature data reported for pure $YMnO_3$ in the HT region (*e.g.* E_a=109.99 kJ/mol in the range 700-900°C [60], 90 kJ/mol for temperatures of 600-1000°C [59] or 93.31 kJ/mol for T>500°C [24].

If on one hand, HT values are similar for pure and Zr-doped compounds, leading us to think that the same process governs the conductivity in the undoped and doped materials, on the other hand, at low temperature, *i.e.* below 550°C, the activation energies are significantly lower and different between non-doped and Zr-doped samples. Such a break in the conductivity slope around 550 °C for $YMnO_3$ has been observed previously, and been suggested to coincide with a ferroelectric transition, [26 65] but the T_C has later been shown to be much higher, ~980-990°C. [66] The aforementioned ability of these materials for storing/releasing oxygen must also plays an important role in the conductivity process change. Indeed, if the oxygen content is modified, structural, occupancy and spin states as well as exchange interaction modifications are expected [60]. Thus, it is possible to think that in the LT

regime, the presence of Mn^{3+}-Mn^{4+} charge carriers is responsible for the electrical conduction of both materials. In fact, it could also explain why the LT activation energy of the Zr-doped compound is lower than that of pure-$YMnO_3$, since the former can absorb more excess oxygen and thus a higher number of carriers participates in the conduction [67]. The electrical conductivity process in the high-temperature range is more difficult to understand since the compounds lose their excess oxygen, and Mn is essentially Mn^{3+}, in both compounds. Then, density of Mn^{4+} carriers (holes) strongly decreases in this range. In such a case, it has been frequently described for transition-metal oxides in literature that the theoretical single valence Mn^{3+} of the compounds exhibits a disproportionation. i.e. simultaneous oxidation and reduction of the transition metal (Mn in our case) as follows [68 69 70]:

$$2Mn^{3+} = Mn^{2+} + Mn^{4+} \qquad (8)$$

If this happens, Mn^{2+} and Mn^{4+} turn in the new charge carriers of the arrangement [71], with the aim to stabilize the ordering structure [72]. In this case, the activation energy necessary for disproportionation of Mn^{3+} (Eq. 8) adds an energy cost in addition to the existing activation energy for the hopping mechanism. This mechanism could explain the difference of behaviour for both materials between HT and LT.

Another interesting point is the higher conductivity of Zr-doped material compared to the pure one, in the entire measured range (σ=1.6 x 10^{-1} S cm^{-1} at 750°C for the former versus 7.4 x10^{-3} S cm^{-1} for the later), see Figure 7a. Two possible hypotheses can be proposed, related either to structural parameters or to oxide ionic conduction. One has to remember that $Y_{0.9}Zr_{0.1}MnO_3$ is present in *P*6_3*/mmc* structure over the whole temperature range, while $YMnO_3$ crystallizes as *P*6_3*cm* at low T and becomes *P*6_3*/mmc* at much higher T. In the latter space group, the MnO_5 bipyramids are not tilted, while in the former an undulation is present. By analogy of what happens for some perovskite-like compounds, in which the non-distorted structures raise the electrical conductivity values [67], the undulation present in the *P*6_3*cm* SG could hinder the movement of carriers in our case. However, as already pointed out, the Zr-doped compound adopts the same *P*6_3*cm* structure at higher temperatures contradicting the previous hypothesis. Additionally, it is worth noting that the Mn-Mn distance in $YMnO_3$ at HT (average ~3.5518 Å) is very similar to that in $Y_{0.9}Zr_{0.1}MnO_{3.05}$ at HT (average ~3.5292 Å) with only ~0.6% of difference.

View Article Online
DOI: 10.1039/C9TA04912F

For that reason, it is possible to propose that the carriers´ mobility, related to the hopping distance, is approximately the same for both compounds. In summary, we believe that structural changes are not responsible for the different electrical conductivity properties. As no structural considerations can explain the difference between the compounds, we believe that the higher σ values for $Y_{0.9}Zr_{0.1}MnO_{3.05}$ are because a large part of the electrical conductivity is not electronic, but ionic (*i.e.* by oxide ions), the main difference between $YMnO_3$ and $Y_{0.9}Zr_{0.1}MnO_{3+\delta}$ is the naturally higher oxygen content. In absence of ionic transport measurements, a discussion concerning this point is given in the following section 3.4.

Finally, more in scope with the application itself, the conductivity of both compounds seems low, compared to perovskite-materials commonly used as SOFC cathodes: LSM (σ~180 S cm^{-1}), LSCF (σ~300-400 S cm^{-1}), BSCF (σ~30 S cm^{-1}) [73] or LBC (σ~300 S cm^{-1}) [74]. In fact, these materials usually exhibit higher conductivity in air (cathodic side) but in anodic atmosphere they hardly reach a conductivity of roughly 1 S cm^{-1}. This apparent problem of poor electrochemical performance is not due to poor electrocatalytic properties but rather to poor conductivity [75]. For that reason, Gorte *et al.* proposed a strategy to improve anode performance despite the low conductivity values of the material. It consists in building one electrode in two layers: the first one is called functional layer and is thin (10-20 μm); it is responsible for the electro-catalytical behaviour. the second (thicker) layer on top of the functional layer is responsible for the current collection. In this kind of electrode configuration, the functional layer requires a minimal conductivity value of only σ~0.01 S cm^{-1}, meanwhile, for the second layer we can use any porous material (CerMets, oxides or metals) with enough electronic conductivity but chemically compatible with the functional layer material [75] [76] [77]. The application of such methodology has already been proved to be efficient, as for instance in the case of a $La_xSr_{1-x}TiO_{3-\delta}$ lamellar anode. In that case, even if the x=0.33 LST3D compound exhibits a conductivity two orders of magnitude higher (σ=8.0 S cm^{-1} at 800°C in reducing atmosphere) than its x=0.8 counterpart LST2D (σ=2.3x10^{-2} S cm^{-1} in same conditions) [78], the electrochemical performance of LST2D material is seven times higher than LST3D, when these materials operate as functional layer with a Nickel current collecting layer [77]. Using this approach, it is of interest to study the electrochemical behaviour of the proposed $Y_{1-x}Zr_xMnO_3$.

View Article Online
DOI: 10.1039/C9TA04912F

3.4. Electrochemical properties

$YMnO_3$ and $Y_{0.9}Zr_{0.1}MnO_3$ were evaluated as potential cathode materials using EIS measurements in air. The evolution with temperature of the impedance data corresponding to the optimal cells prepared with $YMnO_3$ (sintered at 1150°C) and 10%Zr-doped $YMnO_3$ (sintered at 1100°C) are exhibited in Figures 8a and 8b, respectively, using LSM material as current colleting material. Impedance values were normalized considering the electrode area in a symmetric cell and the cell geometry ($Z_{Normalized}=Z_{Measured}$*Electrode geometric area/2). Thus, for both the LSM/$YMnO_3$/YSZ/$YMnO_3$/LSM and LSM/$Y_{0.9}Zr_{0.1}MnO_3$/YSZ/$Y_{0.9}Zr_{0.1}MnO_3$/LSM cells, the spectra present two well distinguished arcs. Nonetheless, the high frequency contribution (frequency higher than 10^1 Hz) disappears from 600°C; therefore, this arc seems to belong to the electrolyte impedance [79]. In this form, only the low frequency contribution can be associated with the Oxygen Reduction Reaction (ORR) at the electrode. On the other hand, the shape of the spectra for the Zr-doped cells are different from pure-$YMnO_3$, probably due to different limiting processes. In each case, such difference will be deeply studied in a forthcoming article, but, from Figures 8a and 8b, it is already possible to conclude that resistances for LSM/$YMnO_3$/YSZ/$YMnO_3$/LSM cell are lower than for LSM/$Y_{0.9}Zr_{0.1}MnO_3$/YSZ/$Y_{0.9}Zr_{0.1}MnO_3$/LSM cells whatever the temperature. A comparison of the Arrhenius plot of the Area-Specific Resistance (ASR) vs temperature evolution for each optimal cells using pure-$YMnO_3$ (sintered at 1150°C) or 10%Zr-doped (sintered at 1100°C) electrode is given in Figure 9 (details concerning the fit of EIS data are given in section 7 of Supplementary Information). It emphasizes the best performance of the $YMnO_3$-based cell (R_P=0.209 Ω cm^2 at 800°C), although it is important to highlight that both sets of values can be considered as high for cathodes (R_P=0.555 Ω cm^2 at 800°C $Y_{0.9}Zr_{0.1}MnO_3$-based cell). For example, the layered cobaltites $NdBaCo_2O_{6-\delta}$ or $SmBaCo_2O_{6-\delta}$ exhibit values of more than one order of magnitude lower for the polarization resistance at 700°C (R_P=0.035 and 0.08 Ω cm^2, respectively). However, our values for the new manganites are lower than the reported for the state of art cathode LSM (R_p<1 Ω cm^2 at 1000°C) or the Ruddlesden-Popper ferrites $Sr_3FeMO_{6+\delta}$ (M= Fe, Co, Ni) (R_P≈1.25-4 Ω cm^2 at 800°C) [41]. Our polarization resistance values are comparable with those of

LSM/YSZ composites 60:40 and 40:60 (0.49 Ω cm^2 and 6.53 Ω cm^2 at 700°C, respectively) [80]. Therefore, being the first reported study on the subject, we can conclude that the electrode proposed in the current work are promising also from the electrochemical point of view. Such activity is possibly related to the particular conduction properties of the material, for which we have strong presumption of Mixed Ionic Electronic Conductivity, as already mentionned above.

To determine how Zr-doping affects the ionic conductivity in $Y_{1-x}Zr_xMnO_{3+\delta}$, we investigate how doping affect the migration energy barriers of oxygen interstitials. Following the work by Skjærvø *et al.* [58], the oxygen interstitials are migrating through an interstitialcy mechanism in the *ab*-plane, where two distinct migration paths can be identified. The first path, hereby referred to as path (1), corresponds to nudging of the planar O3 site above the Y1-site, and the second path, hereby referred to as path (2), corresponds to nudging of the planar O4 site below the Y2-site. The two migration paths are illustrated in the inset crystal structure in Figure 6c. The resulting migration energy barriers for O_i in $YMnO_{3+\delta}$ are 0.49 eV and 0.65 eV for path (1) and (2), respectively, in agreement with Skjærvø *et al.*. [58] The migration energy path for O_i in $Y_{1-x}Zr_xMnO_{3+\delta}$ are also comparable to that of O_i in $YMnO_{3+\delta}$, with resulting migration energy barriers of O_i in the vicinity of Zr_{Y1} and Zr_{Y2} of 0.30 eV and 0.69 eV, respectively. Note that for the results for migrating O_i in the vicinity of Zr_{Y1}, the initial and final structures are not the energy minimum along the migration path. This can be explained by the localization of the charge compensating holes, where in the initial and final structures they are partially localized on two Mn close to O_i, while along the rest of the migration path they are localized on one Mn. This is an artefact of the DFT calculations, where the latter is expected to give an energy lowering. Hence, the migration energy barrier assuming localized holes on one Mn for the initial and final structures is expected to be higher, with an expected value similar to that of path (1).

The mobility of oxygen ions in Zr-doped $Y_{1-x}Zr_xMnO_{3+\delta}$ is thus expected to be at least as good as pure $YMnO_{3+\delta}$, and Zr-doping might even induce a migration path with significantly lower energy barrier, 0.30 vs 0.49 eV, however with some uncertainties. Hence, the observed enhanced conductivity of $Y_{0.9}Zr_{0.1}MnO_{3.05}$ compared to $YMnO_3$ could indeed be caused by a higher oxygen content, as well as a possibly higher oxygen ion mobility.

4. Conclusions

For the first time, materials of the $Y_{1-X}Zr_xMnO_{3+\delta}$ series with layered hexagonal crystal structure different from the perovskite framework have been in depth studied for a possible use as SOFC cathode. The 2D structure associated to a particular coordination of the transition metal, corresponding to [MnO_5] bi-pyramids instead of classical octahedra in the perovskite, results in a peculiar aptitude of the framework for oxygen uptake, especially at low temperature. By adequate doping of Zr for Y, we were able to maintain such oxygen excess, as interstitial atoms Oi located in the equatorial plane of the bi-pyramids, Mn reduction to Mn^{2+} being energetically unfavourable, as proved both experimentally and using DFT calculations. The main consequence is a possible MIEC behaviour in Zr-doped $YMnO_3$, suggested by both conductivity measurements and, again, theoretical calculations. Determination of ionic transport number is currently under study and will confirm such strong presumptions, but EIS first measurements are already very promising for the application; detailed electrocatalytic performance of the series will be published soon to complete the present article. As a final comment, where most of the electrodes based on La/Sr transition metal oxides have to be protected from YSZ by a buffer layer, the use of $YMnO_3$-based materials exhibits an additional advantage on the technological and cost point of view, considering the absence of chemical reactivity with traditional YSZ electrolyte, as recently reported by our group. [35]

Acknowledgments

The authors acknowledge the financial support of the Colombian Administrative Department of Science, Technology and Innovation COLCIENCIAS (Project # 110265842833 "*Symmetrical high temperature Fuel Cell operating with Colombian natural gas*" (contract # 038-2015) and Project "S*tudy of nanostructured mixed oxides with layered crystal structure as electrode materials for Solid Oxide fuel Cells*" (contract # RC 611-2014)), UIS' Vicerrectorship for Investigation and Extension (Projects # 9448 and # 9449), CNRS, Région Haut de France and European FEDER funds as well as the technical support of UIS' X-Ray Laboratory (Parque Tecnológico Guatiguará) for XRD measurements. Florence Porcher (LLB Saclay, France) is thanked for Neutron Diffraction Data Collection. Zulma Moreno Botello acknowledges UIS and in particular the School of Metallurgy and Materials

Science for the Ph.D. scholarship. The authors express their personal thanks to Houria Kabbour and Edouard Capoen from UCCS (Lille) for useful discussions and participation in conductivity measurements, respectively, as well as Mario Macías and Monica Sandoval from UIS, and Liliana Mogni, Jesús Vega and Diana Garcés from CNEA/CAB for their technical advices. DRS and SMS acknowledges support from the Research Council of Norway (FRINATEK Project No. 231430/F20) and computational resources provided by Uninett Sigma2 through projects NN9264K and ntnu243.

Figure Captions

Figure 1. (a) Hexagonal *P6$_3$cm* structure of $YMnO_3$ showing the buckled laminar arrangement of tilted MnO_5 trigonal bi-pyramids joined by corners. (b) partial view of $YMnO_{3+\delta}$ *R*3*c* superstructure showing the oxygen interstitial site O6 (in yellow) within the a-b plane around the Mn sites. (c) 8-fold coordination of Mn1 in *Pca*2$_1$ structure of $YMnO_{3+\delta}$ with additional O5-x interstitial sites (in yellow) (d) Simulated X-Ray Diffraction patterns (using Cu-$K_{\alpha 1\text{-}2}$ incident radiation) for $YMnO_{3+\delta}$ compounds in their different possible structural arrangements. The arrow indicates the reflection at 2θ~23° in the *P*6$_3$*cm* pattern which is absent for the *P*6$_3$*/mmc* symmetry. Adapted from [16] [30].

Figure 2. X-Ray diffraction patterns of $Y_{1-x}Zr_xMnO_3$ ($0 \le x \le 0.15$) indexed in *P*6$_3$*cm* structure. Reproduced with permission from [35].

Figure 3. Thermogravimetrical analysis (TGA) measurements of oxygen content for $Y_{0.9}Zr_{0.1}MnO_3$ and $YMnO_3$ as a function of temperature in air (heating and cooling rates= 0.2°C min^{-1}).

Figure 4. X-Ray diffraction patterns of $YMnO_3$ and $Y_{0.9}Zr_{0.1}MnO_3$ synthesized by the Pechini method (with (*hkl)* indices).

Figure 5. Representation along *c* axis of *P*6$_3$*/mmc* $Y_{0.9}Zr_{0.1}MnO_{3+\delta}$ structure evidencing the position of overstoichiometric O3 atoms (in yellow) in the normally empty hexagonal cavities defined by three MnO_5 bipyramids. Y atoms have been omitted for clarity.

View Article Online
DOI: 10.1039/C9TA04912F

Figure 6. (a) Calculated defect formation energies for adding one oxygen interstitial per 120 atom supercell in stoichiometric and Zr-doped $YMnO_3$. (b) Resulting changes in the electronic DOSes by introducing O_i in stoichiometric and Zr-doped $YMnO_3$. (c) Calculated migration energy barriers for O_i in stoichiometric and Zr-doped $YMnO_3$. The assumed migration paths (1) and (2) are illustrated in the inset crystal structure.

Figure 7. (a) Evolution with the temperature of the electrical conductivity of $YMnO_3$ and $Y_{0.9}Zr_{0.1}MnO_{3+\delta}$ compounds in air. (b) Arrhenius plot of the electrical conductivity evolution with the temperature for $YMnO_3$ (purple triangles) and $Y_{0.9}Zr_{0.1}MnO_{3+\delta}$ (orange triangles) in air.

Figure 8. Impedance spectra at different temperatures in air of (a) LSM/$YMnO_3$/YSZ/$YMnO_3$/LSM cell (sintered at 1150°C) and (b) LSM/$Y_{0.9}Zr_{0.1}MnO_3$/YSZ/$Y_{0.9}Zr_{0.1}MnO_3$/LSM cell (sintered at 1100°C).

Figure 9. Log ASR values vs temperature for symmetrical cells containig $YMnO_3$ and $Y_{0.9}Zr_{0.1}MnO_3$ compound is its optimal conditions.

References

1 J. T. S. Irvine and P. A. Connor, *Solid oxide fuels cells : facts and figures : past, present and future perspectives for SOFC technologies*, Springer, 2013.

2 Z. Shao and M. O. Tadé, *Intermediate-Temperature Solid Oxide Fuel Cells: Materials and Applications*, Springer, Berlin, Heidelberg, 2016.

3 N. Minh, J. Mizusaki and S. C. Singhal, *ECS Trans.*, 2017, **78**, 63–73.

4 H. Tu and U. Stimming, *J. Power Sources*, 2004, **127**, 284–293.

5 M. M. Kuklja, E. A. Kotomin, R. Merkle, Y. A. Mastrikov and J. Maier, *Phys. Chem. Chem. Phys.*, 2013, **15**, 5443.

6 Y. Chen, W. Zhou, D. Ding, M. Liu, F. Ciucci, M. Tade and Z. Shao, *Adv. Energy Mater.*, 2015, **5**, 1500537.

7 V. Miguel-Perez, J. P. Ouweltjes, A. Tarancon, M. Torrell, V. Bongiorno, Z.

Wuillemin, D. Montinaro and A. Morata, *ECS Trans.*, 2015, **68(1)**, 1803-1813.

8 F. S. da Silva and T. M. de Souza, *Int. J. Hydrogen Energy*, 2017, **42**, 26020–26036.

9 Z. Yang, M. Guo, N. Wang, C. Ma, J. Wang and M. Han, *Int. J. Hydrogen Energy*, 2017, **42**, 24948–24959.

10 J. H. Zhu and H. Ghezel-Ayagh, *Int. J. Hydrogen Energy*, 2017, **42**, 24278–24300.

11 T. Ishihara, *Perovskite oxide for solid oxide fuel cells*, Springer, 2009.

12 J. M. D. Coey, M. Viret and S. von Molnár, *Adv. Phys.*, 1999, **48**, 167–293.

13 Y. D. Tretyakov, E. A. Goodilin, D. V Peryshkov and D. M. Itkis, *Russ. Chem. Rev.*, 2004, **73**, 881–898.

14 V. F. Balakirev and Y. V. Golikov, *Inorg. Mater.*, 2006, **42**, S49–S69.

15 S. Remsen and B. Dabrowski, *Chem. Mater.*, 2011, **23**, 3818–3827.

16 C. Abughayada, B. Dabrowski, S. Kolesnik, D. E. Brown and O. Chmaissem, *Chem. Mater.*, 2015, **27**, 6259–6267.

17 A. Klimkowicz, K. Cichy, O. Chmaissem, B. Dabrowski, B. Poudel, K. Świerczek, K. M. Taddei and A. Takasaki, *J. Mater. Chem. A*, 2019, **7**, 2608–2618.

18 B. B. Van Aken, A. Meetsma and T. T. M. Palstra, *Acta Crystallogr. Sect. E Struct. Reports Online*, 2001, **57**, i101–i103.

19 A. S. Gibbs, K. S. Knight and P. Lightfoot, *Phys. Rev. B*, 2011, **83**, 094111.

20 H. L. Yakel, *Acta Crystallogr.*, 1955, **8**, 394–398.

21 H. L. Yakel Jnr, W. C. Koehler, E. F. Bertaut and E. F. Forrat, *Acta Crystallogr.*, 1963, **16**, 957–962.

22 Q. H. Zhang, X. Shen, Y. Yao, Y. G. Wang, C. Q. Jin and R. C. Yu, *J. Alloys Compd.*, 2015, **648**, 253–257.

23 A. Veres, J. G. Noudem, S. Fourrez and G. Bailleul, *Solid State Sci.*, 2006, **8**, 137–141.

24 P. Ren, H. Fan and X. Wang, *Appl. Phys. Lett.*, 2013, **103**, 152905.

25 A. E. Smith, A. W. Sleight and M. A. Subramanian, *Mater. Res. Bull.*, 2011, **46**, 1–5.

26 U. Salazar-Kuri, M. E. Mendoza and J. M. Siqueiros, *Phys. B Condens. Matter*, 2012, **407**, 3551–3554.

27 M. Tomczyk, P. Maria Vilarinho, A. Moreira and A. Almeida, *J. Appl. Phys.*, 2011, **110**, 064116.

28 S. Mori, J. Tokunaga, Y. Horibe, Y. Aikawa and T. Katsufuji, *Phys. Rev. B*, 2005, **72**, 224434.

29 S. Mori, J. Tokunaga, Y. Horibe, Y. Aikawa and T. Katsufuji, *Jpn. J. Appl. Phys.*, 2005, **44**, 7174–7176.

30 C. Abughayada, B. Dabrowski, M. Avdeev, S. Kolesnik, S. Remsen and O. Chmaissem, *J. Solid State Chem.*, 2014, **217**, 127–135.

31 S. Remsen, B. Dabrowski, O. Chmaissem, J. Mais and A. Szewczyk, *J. Solid State Chem.*, 2011, **184**, 2306–2314.

32 I. Levin, V. Krayzman, T. A. Vanderah, M. Tomczyk, H. Wu, M. G. Tucker, H. Y. Playford, J. C. Woicik, C. L. Dennis and P. M. Vilarinho, *J. Solid State Chem.*, 2017, **246**, 29–41.

33 B. B. Van Aken, J.-W. G. Bos, R. A. de Groot and T. T. M. Palstra, *Phys. Rev. B*, 2001, **63**, 125127.

34 T. Katsufuji, M. Masaki, A. Machida, M. Moritomo, K. Kato, E. Nishibori, M. Takata, M. Sakata, K. Ohoyama, K. Kitazawa and H. Takagi, *Phys. Rev. B*, 2002, **66**, 134434.

35 Z. L. Moreno Botello, A. Caneiro, P. Roussel and G. Gauthier, *J. Alloys Compd.*, 2017, **690**, 348–355.

View Article Online
DOI: 10.1039/C9TA04912F

36 J. Rodríguez-Carvajal, *Phys. B Condens. Matter*, 1993, **192**, 55–69.

37 T. Roisnel and J. Rodriguez-Carvajal, in *Materials Science Forum, Proceedings of the Seventh European Powder Diffraction Conference (EPDIC 7)*, ed. R. Delhez and E.J. Mittenmeijer, 2000, pp. 118–123.

38 J. F. Bérar and P. Lelann, *J. Appl. Crystallogr.*, 1991, **24**, 1–5.

39 V. Petříček, M. Dušek and L. Palatinus, *Zeitschrift für Krist. - Cryst. Mater.*, 2015, **229**, 345-352.

40 K. Momma, T. Ikeda, A. A. Belik and F. Izumi, *Powder Diffr.*, 2013, **28**, 184–193.

41 L. V. Mogni, Instituto Balseiro, Bariloche, Argentina, 2007.

42 M. Zahid, I. Arul Raj, F. Tietz, P. Lersch and D. Stöver, *ECS Proc. Vol.*, 2005, **2005**–**07**, 1708–1716.

43 P. E. Blöchl, *Phys. Rev. B*, 1994, **50**, 17953–17979.

44 G. Kresse and J. Furthmüller, *Phys. Rev. B*, 1996, **54**, 11169–11186.

45 G. Kresse and D. Joubert, *Phys. Rev. B*, 1999, **59**, 1758–1775.

46 J. P. Perdew, A. Ruzsinszky, G. I. Csonka, O. A. Vydrov, G. E. Scuseria, L. A. Constantin, X. Zhou and K. Burke, *Phys. Rev. Lett.*, 2008, **100**, 136406.

47 C. Degenhardt, M. Fiebig, D. Fröhlich, T. Lottermoser and R. V. Pisarev, *Appl. Phys. B*, 2001, **73**, 139–144.

48 S. L. Dudarev, G. A. Botton, S. Y. Savrasov, C. J. Humphreys and A. P. Sutton, *Phys. Rev. B*, 1998, **57**, 1505–1509.

49 J. E. Medvedeva, V. I. Anisimov, M. A. Korotin, O. N. Mryasov and A. J. Freeman, *J. Phys. Condens. Matter*, 2000, **12**, 304.

50 S. H. Skjærvø, E. T. Wefring, S. K. Nesdal, N. H. Gaukås, G. H. Olsen, J. Glaum, T. Tybell and S. M. Selbach, *Nat. Commun.*, 2016, **7**, 13745.

51 G. Henkelman, B. P. Uberuaga and H. Jónsson, *J. Chem. Phys.*, 2000, **113**,

View Article Online
DOI: 10.1039/C9TA04912F

9901–9904.

52 G. Henkelman and H. Jónsson, *J. Chem. Phys.*, 2000, **113**, 9978–9985.

53 R. D. Shannon, *Acta Crystallogr. Sect. A*, 1976, **32**, 751–767.

54 C. Zhang, X. Zhang, Y. Sun and S. Liu, *Phys. Rev. B*, 2011, **83**, 054104.

55 K. Momma, F. Izumi and IUCr, *J. Appl. Crystallogr.*, 2011, **44**, 1272–1276.

56 H. Kabbour, G. H. Gauthier, F. Tessier, M. Huvé, T. Pussacq, P. Roussel, M. A. Hayward, Z. L. B. Moreno, M. Marinova, M. Colmont, S. Colis and O. Mentré, *Inorg. Chem.*, 2017, **56**, 8547–8553.

57 T. Grande, J. R. Tolchard and S. M. Selbach, *Chem. Mater.*, 2012, **24**, 338-345.

58 S. H. Skjærvø, E. T. Wefring, S. K. Nesdal, N. H. Gaukås, G. H. Olsen, J. Glaum, T. Tybell and S. M. Selbach, *Nat. Commun.*, 2016, **7**, 13745.

59 G. Lescano, F. M. Figueiredo, F. M. B. Marques and J. Schmidt, *J. Eur. Ceram. Soc.*, 2001, **21**, 2037–2040.

60 S. Remsen, Northern Illinois University, DeKalb (IL), USA, 2011.

61 L. Jeuvrey, O. Peña, A. Moure and C. Moure, *J. Magn. Magn. Mater.*, 2012, **324**, 717–722.

62 I. H. Ismailzade, G. A. Smolenskii, V. I. Nesterenko and F. A. Agaev, *Phys. Status Solidi*, 1971, **5**, 83–89.

63 C. Moure, J. F. Fernandez, M. Villegas and P. Duran, *J. Eur. Ceram. Soc.*, 1999, **19**, 131–137.

64 J. Palma, J. R. Jurado, P. Duran and C. Pascual, *Boletines Soc. Cerámica y Vidr.*, 1991, **30**, 472.

65 G. V. Subba Rao, B. M. Wanklyn and C. N. R. Rao, *J. Phys. Chem. Solids*, 1971, **32**, 345–358.

66 M. Lilienblum, T. Lottermoser, S. Manz, S. M. Selbach, A. Cano, M. Fiebig,

View Article Online
DOI: 10.1039/C9TA04912F

Nat. Phys., 2015, **11**, 1070-1073.

67 E. Lay, L. Dessemond and G. Gauthier, *J. Power Sources*, 2013, **221**, 149–156.

68 S. I. Elkalashy, T. V. Aksenova, A. S. Urusova and V. A. Cherepanov, *Solid State Ionics*, 2016, **295**, 96–103.

69 W. T. Fu, *Phys. C Supercond.*, 1995, **250**, 67–74.

70 V. L. Kozhevnikov, I. A. Leonidov, E. B. Mitberg, M. V. Patrakeev, A. N. Petrov and K. R. Poeppelmeier, *J. Solid State Chem.*, 2003, **172**, 296–304.

71 M. Kuznecov, P. Otschik, N. Trofimenko and K. Eichler, *Russ. J. Electrochem.*, 2004, **40**, 1162–1169.

72 P. M. Woodward, D. E. Cox, E. Moshopoulou, A. W. Sleight and S. Morimoto, *Phys. Rev. B*, 2000, **62**, 844–855.

73 D. Rembelski, J. P. Viricelle, L. Combemale and M. Rieu, *Fuel Cells*, 2012, **12**, 256–264.

74 D. A. Garcés, Instituto Balseiro, Bariloche, Argentina, 2014.

75 M. D. Gross, J. M. Vohs and R. J. Gorte, *J. Mater. Chem.*, 2007, **17**, 3071.

76 M. D. Gross, J. M. Vohs and R. J. Gorte, *J. Electrochem. Soc.*, 2007, **154**, B694.

77 C. Périllat-Merceroz, P. Roussel, R.-N. Vannier, P. Gélin, S. Rosini and G. Gauthier, *Adv. Energy Mater.*, 2011, **1**, 573–576.

78 C. Périllat-Merceroz, P. Roussel, M. Huvé, E. Capoen, R.-N. Vannier and G. Gauthier, *Solid State Ionics*, 2013, **247**–**248**, 76–85.

79 L. Baqué, Instituto Balseiro, Bariloche, Argentina, 2011.

80 B. Shri Prakash, S. Senthil Kumar and S. T. Aruna, *Bull. Mater. Sci.*, 2017, **40**, 441–452.

View Article Online
DOI: 10.1039/C9TA04912F

Table 1. Structural parameters for $Y_{0.9}Zr_{0.1}MnO_{3+\delta}$ (RT) with an additional interstitial position O3 position (S.G. $P6_3/mmc$; lattice parameters: a=3.5506(1) Å, c=11.2559(4) Å).

Atom	**Wyckoff position**	***x***	***y***	***z***	**Occupancy**	**U_{eq}**
Y	4e	0	0	0.0214(3)	0.45	0.0151(8)
Zr	4e	0	0	0.0214(3)	0.05	0.0151(8)
Mn	2c	1/3	2/3	1/4	1	0.0197(5)
O1	4f	1/3	2/3	0.0847(1)	1	0.0144(2)
O2	2b	0	0	1/4	0.85954	0.0416(8)
O3*	6h	0.4883(2)	0.2441	1/4	0.135244	0.0668(6)
Reliability factors		**Neutrons**	R_p(%)=2.84, R_{wp}=3.55, GOF=1.94, R_B=7.88			
		X-Ray	R_p(%)=4.90, R_{wp}=6.31, GOF=1.34, R_B=9.23			

View Article Online
DOI: 10.1039/C9TA04912F

Table 2. Activation energy of the electrical conduction process for $YMnO_3$ and $Y_{0.9}Zr_{0.1}MnO_{3+\delta}$ in air.

Sample	Temperature (°C)	Activation energy		
		(eV)	(kJ/mol)	R^2
$YMnO_3$	490-550	0.7680(3)	74.10(3)	0.9968
	550-800	0.9664(4)	93.24(4)	0.9996
$Y_{0.9}Zr_{0.1}MnO_3$	430-570	0.6282(2)	60.61(2)	0.9916
	570-770	1.0396(9)	100.31(9)	0.9998

View Article Online
DOI: 10.1039/C9TA04912F

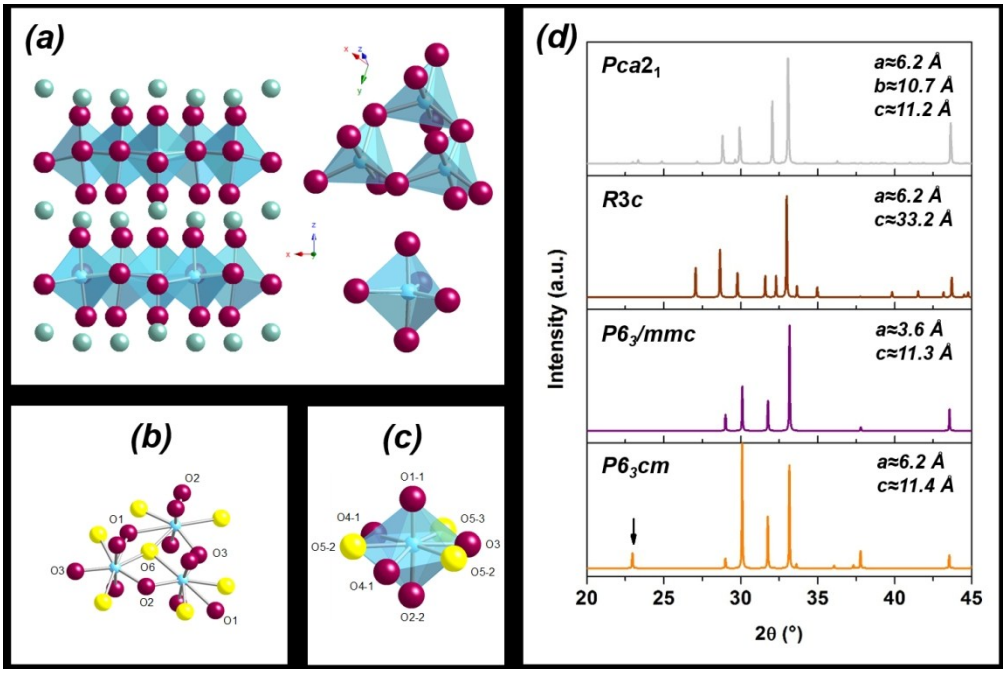

Figure 1. (a) Hexagonal P63cm structure of YMnO3 showing the buckled laminar arrangement of tilted MnO5 trigonal bi-pyramids joined by corners. (b) partial view of YMnO3+δ R3c superstructure showing the oxygen interstitial site O6 (in yellow) within the a-b plane around the Mn sites. (c) 8-fold coordination of Mn1 in Pca21 structure of YMnO3+δ with additional O5-x interstitial sites (in yellow) (d) Simulated X-Ray Diffraction patterns (using Cu-Kα1-2 incident radiation) for YMnO3+δ compounds in their different possible structural arrangements. Adapted from 16 30.

250x166mm (150 x 150 DPI)

View Article Online
DOI: 10.1039/C9TA04912F

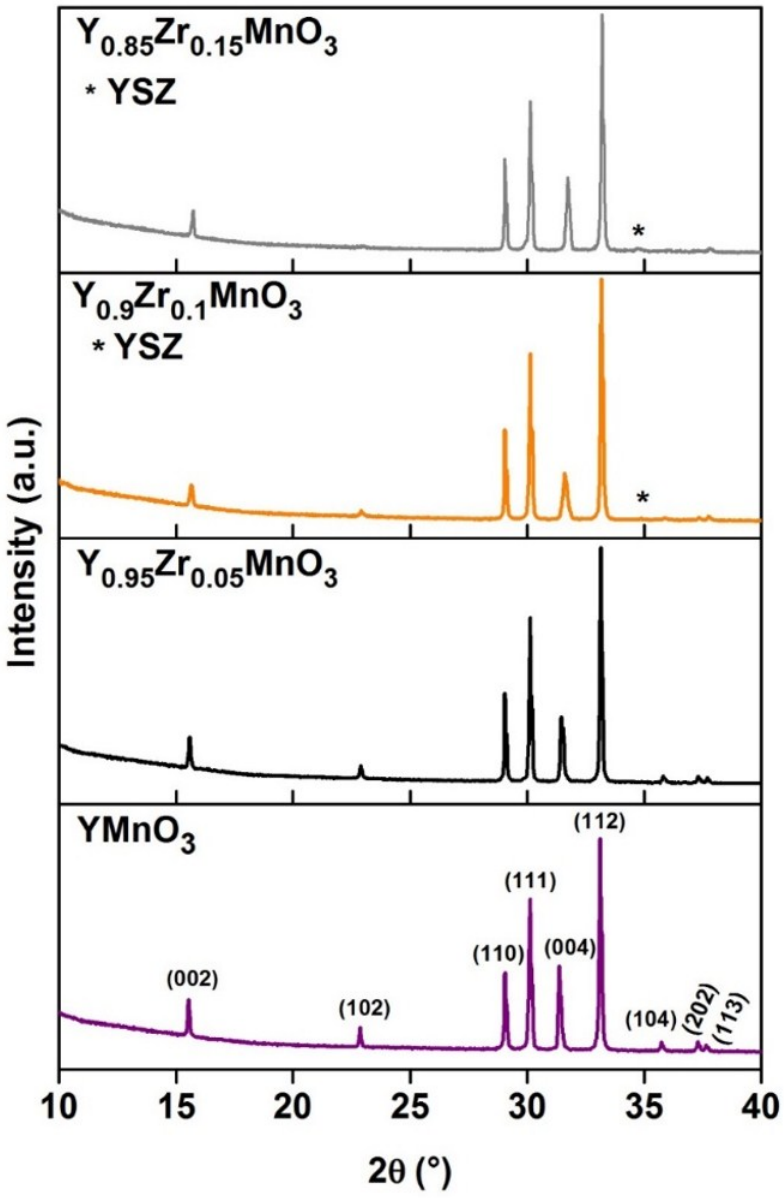

Figure 2. X-Ray diffraction patterns of Y1-xZrxMnO3 (0≤x≤0.15) indexed in P63cm structure. Reproduced with permission from 35.

115x169mm (150 x 150 DPI)

View Article Online
DOI: 10.1039/C9TA04912F

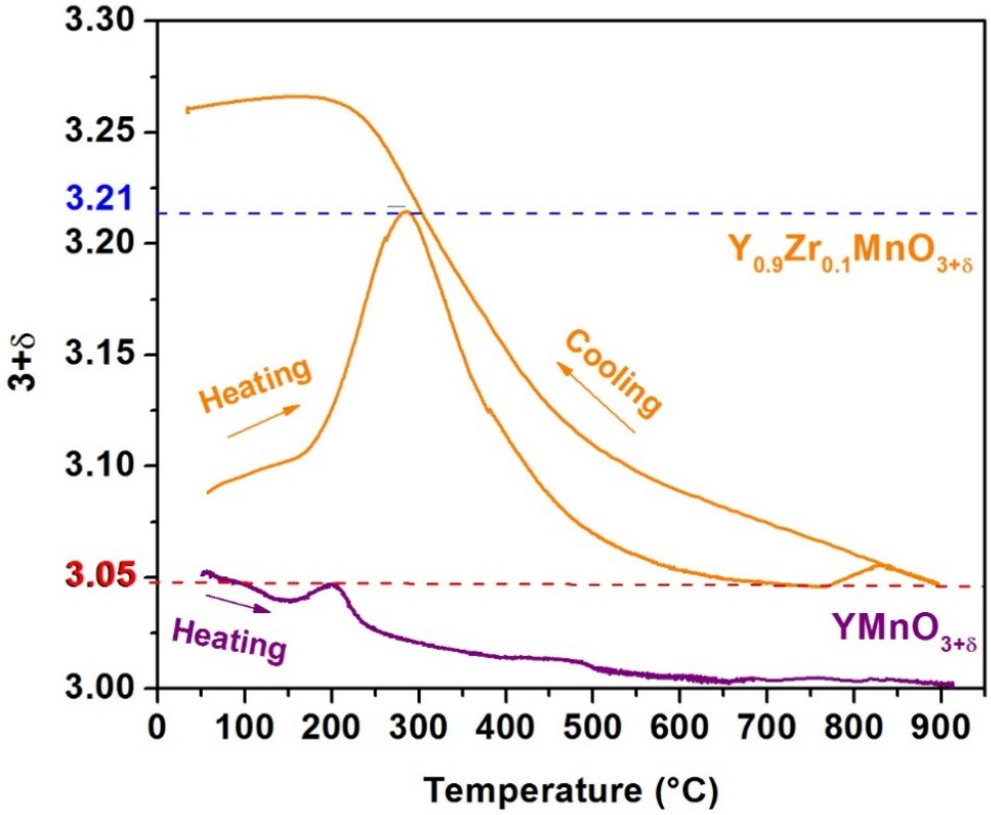

Figure 3. Thermogravimetrical analysis (TGA) measurements of oxygen content for Y0.9Zr0.1MnO3 and YMnO3 as a function of temperature in air (heating and cooling rates= 0.2°C min-1).

165x137mm (150 x 150 DPI)

View Article Online
DOI: 10.1039/C9TA04912F

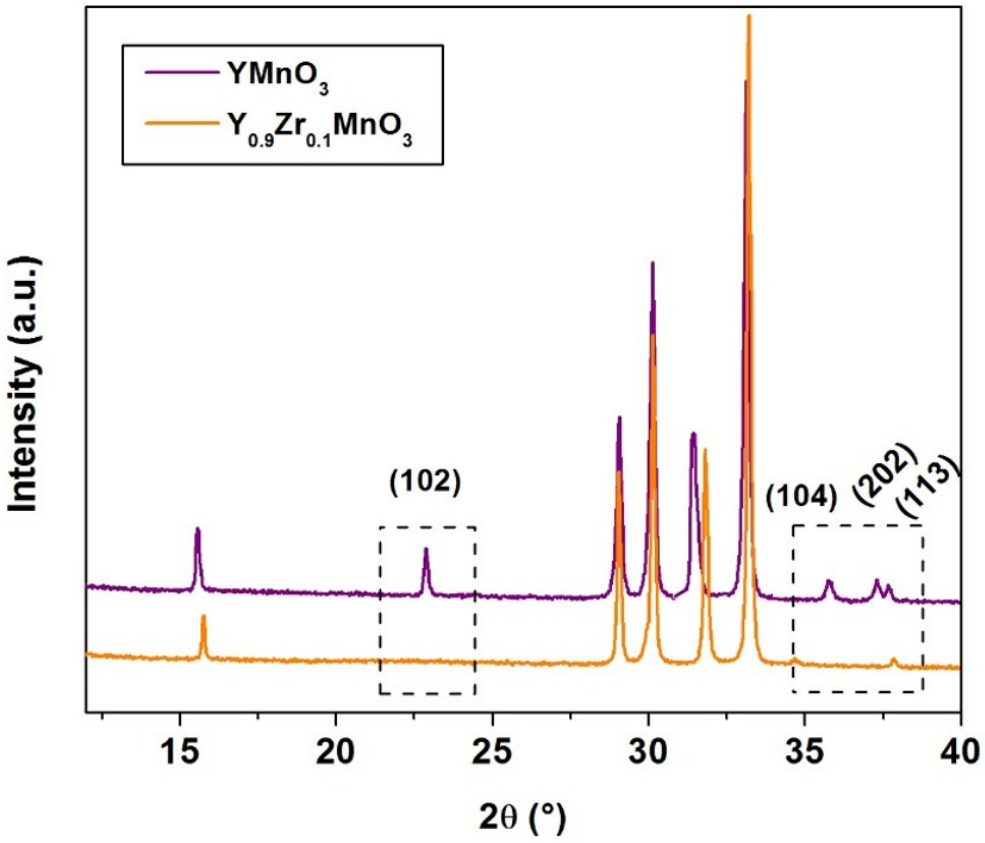

Figure 4. X-Ray diffraction patterns of YMnO3 and Y0.9Zr0.1MnO3 synthesized by the Pechini method (with (hkl) indices).

142x122mm (150 x 150 DPI)

View Article Online
DOI: 10.1039/C9TA04912F

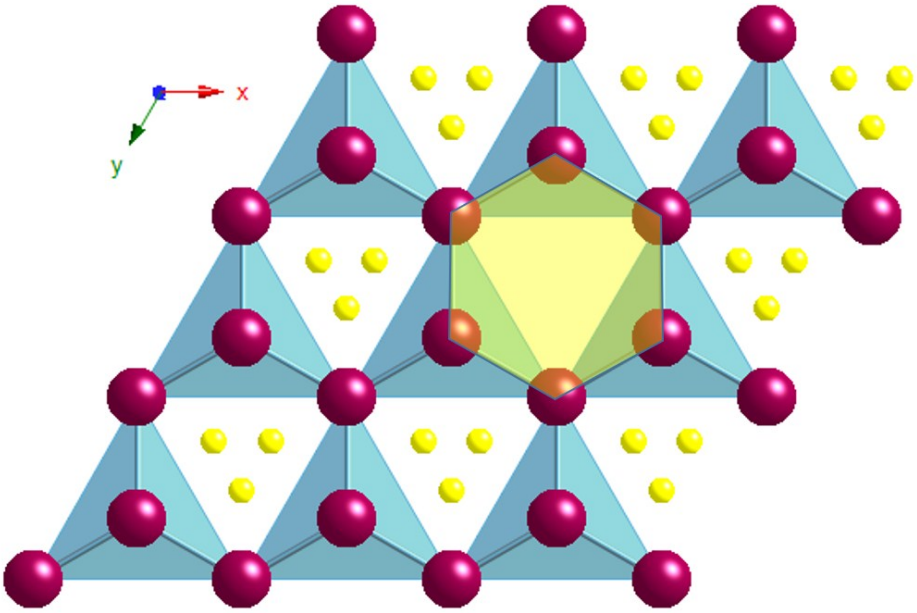

Figure 5. Representation along c axis of P63/mmc Y0.9Zr0.1MnO3+δ structure evidencing the position of overstoichiometric O3 atoms (in yellow) in the normally empty hexagonal cavities defined by three MnO5 bipyramids. Y atoms have been omitted for clarity.

183x123mm (150 x 150 DPI)

View Article Online
DOI: 10.1039/C9TA04912F

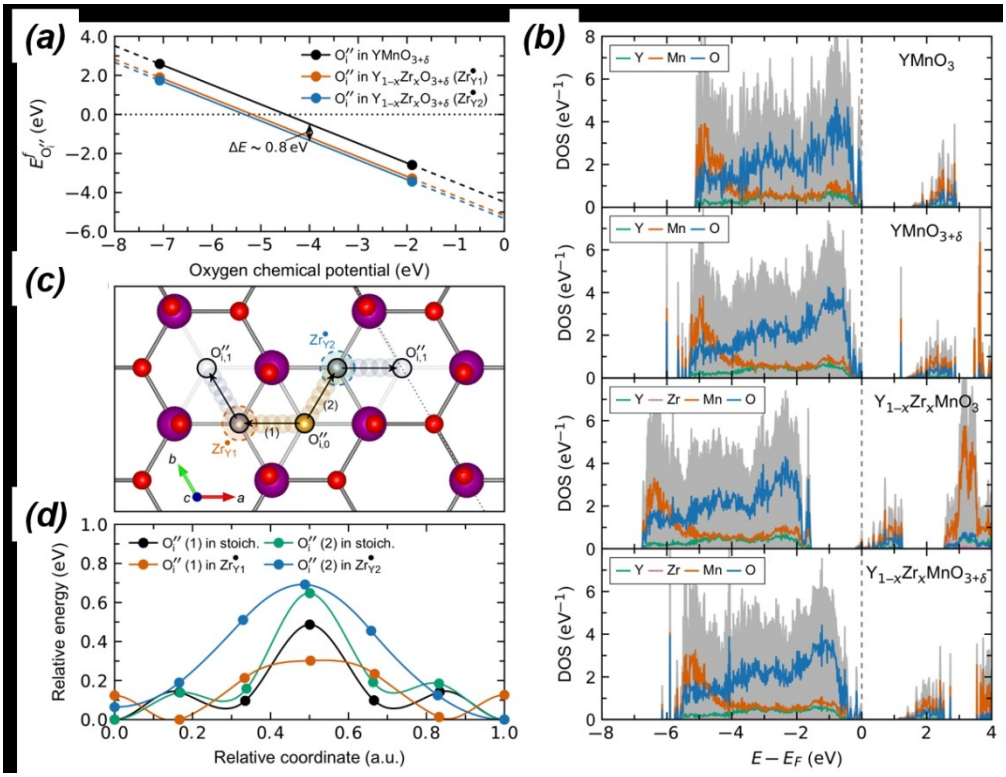

Figure 6. (a) Calculated defect formation energies for adding one oxygen interstitial per 120 atom supercell in stoichiometric and Zr-doped YMnO3. (b) Resulting changes in the electronic DOSes by introducing Oi in stoichiometric and Zr-doped YMnO3. (c) Calculated migration energy barriers for Oi in stoichiometric and Zr-doped YMnO3. The assumed migration paths (1) and (2) are illustrated in the inset crystal structure.

205x157mm (150 x 150 DPI)

View Article Online
DOI: 10.1039/C9TA04912F

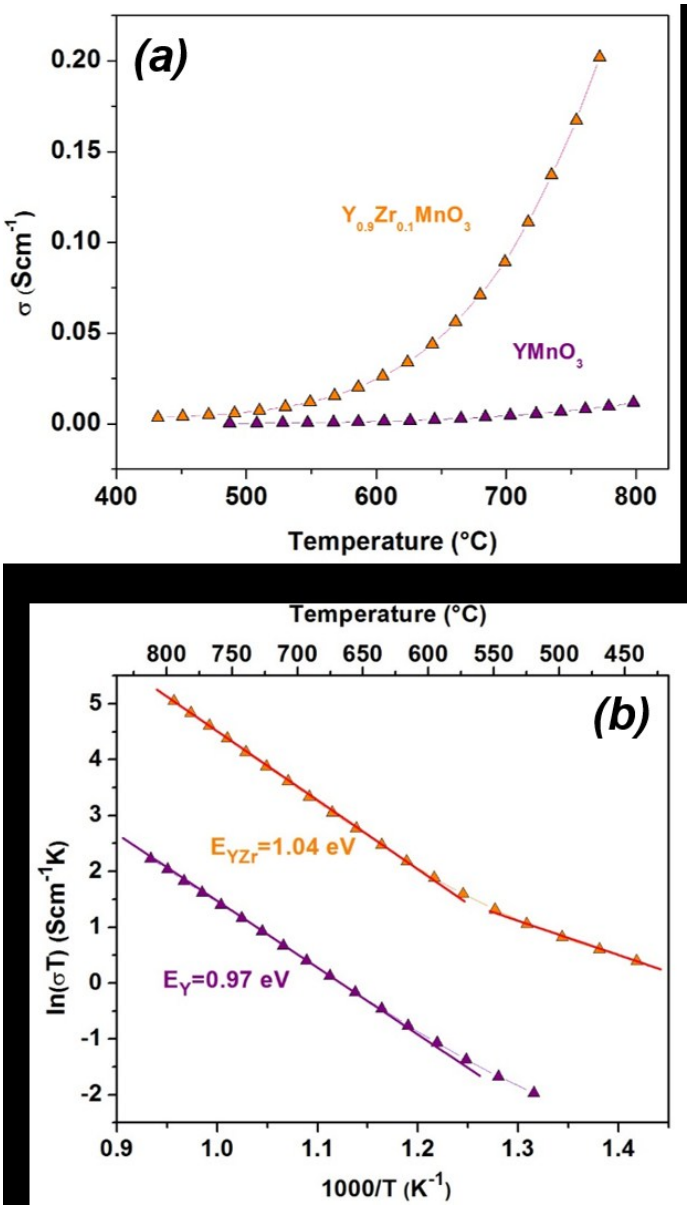

Figure 7. (a) Evolution with the temperature of the electrical conductivity of YMnO3 and Y0.9Zr0.1MnO3+δ compounds in air. (b) Arrhenius plot of the electrical conductivity evolution with the temperature for YMnO3 (purple triangles) and Y0.9Zr0.1MnO3+δ (orange triangles) in air.

104x183mm (150 x 150 DPI)

View Article Online
DOI: 10.1039/C9TA04912F

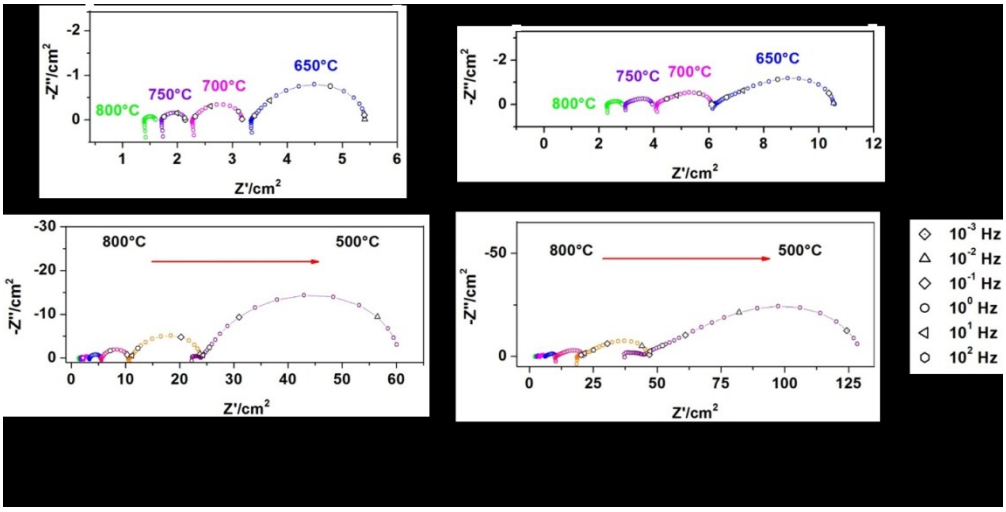

Figure 8. Impedance spectra at different temperatures in air of (a) LSM/YMnO3/YSZ/YMnO3/LSM cell (sintered at 1150°C) and (b) LSM/Y0.9Zr0.1MnO3/YSZ/Y0.9Zr0.1MnO3/LSM cell (sintered at 1100°C).

238x119mm (150 x 150 DPI)

View Article Online
DOI: 10.1039/C9TA04912F

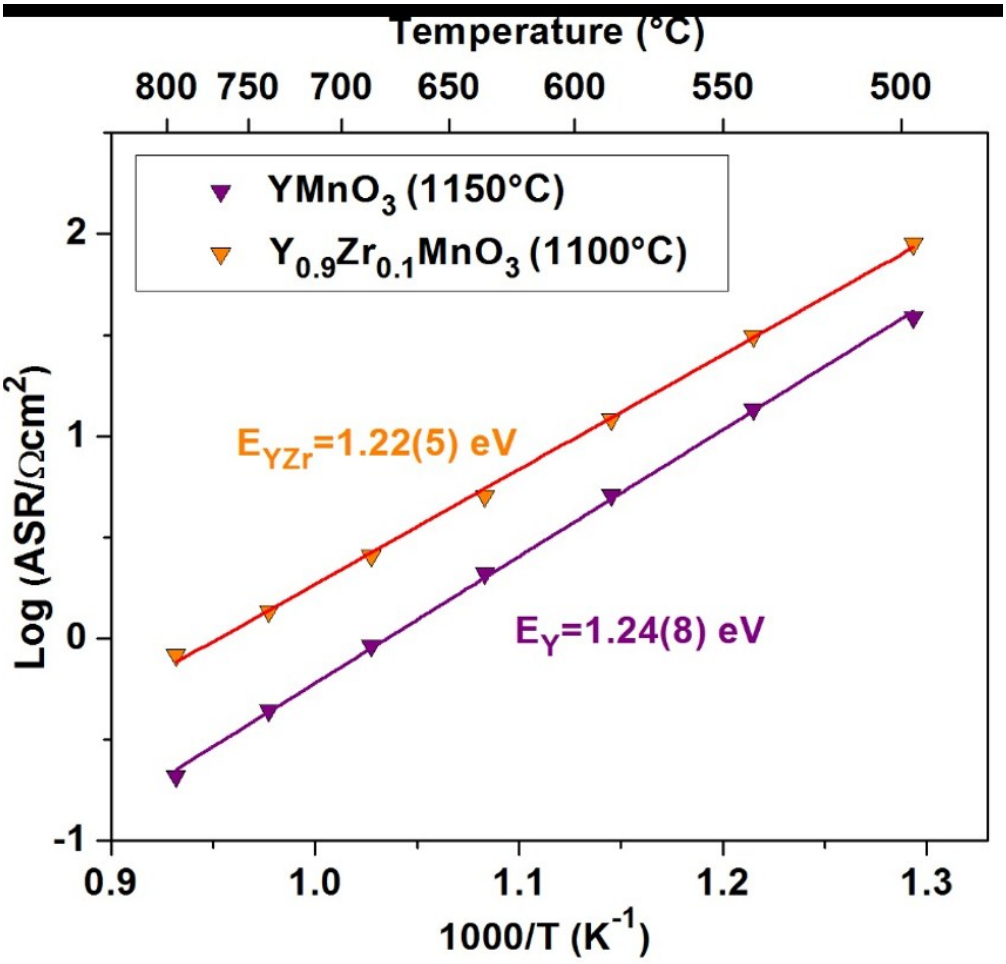

Figure 9. Log ASR values vs temperature for symmetrical cells containig YMnO3 and Y0.9Zr0.1MnO3 compound is its optimal conditions.

144x138mm (150 x 150 DPI)

View Article Online
DOI: 10.1039/C9TA04912F

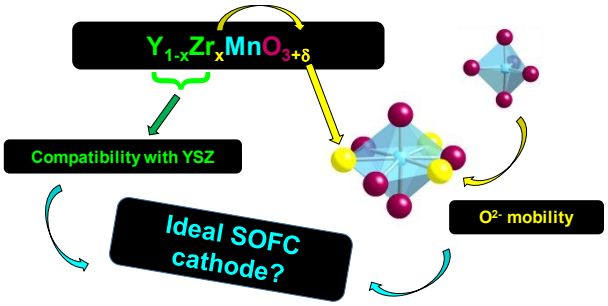

Zr doping stabilizes interstitial oxygen in layered manganite $YMnO_3$ and provides O^{2-} migration path with lower energy barrier. The resulting material is of highest interest as a YSZ compatible SOFC cathode.